The Astrophysical Journal Letters, 839:L11 (8pp), 2017 April 10 https://doi.org/10.3847/2041-8213/aa69be

A Very Large ($\theta_E \gtrsim 40''$) Strong Gravitational Lens Selected with the Sunyaev–Zel'dovich Effect: PLCK G287.0+32.9 ($z = 0.38$)

Adi Zitrin[1], Stella Seitz[2,3], Anna Monna[2,3], Anton M. Koekemoer[4], Mario Nonino[5], Daniel Gruen[6,7,10], Italo Balestra[2,5], Marisa Girardi[5,8], Johannes Koppenhoefer[2,3], and Amata Mercurio[9]
[1] Physics Department, Ben-Gurion University of the Negev, P.O. Box 653, Be'er-Sheva 8410501, Israel; adizitrin@gmail.com
[2] University Observatory Munich, Scheinerstrasse 1, D-81679 Munich, Germany
[3] Max Planck Institute for Extraterrestrial Physics, Giessenbachstrasse, D-85741 Garching, Germany
[4] Space Telescope Science Institute, 3700 San Martin Drive, Baltimore, MD 21218, USA
[5] INAF—Osservatorio Astronomico di Trieste, via G. B. Tiepolo 11, I-34131 Trieste, Italy
[6] SLAC National Accelerator Laboratory, Menlo Park, CA 94025, USA
[7] KIPAC, Physics Department, Stanford University, Stanford, CA 94305, USA
[8] Dipartimento di Fisica, Universitá degli Studi di Trieste, Via Tiepolo 11, I-34143 Trieste, Italy
[9] INAF—Osservatorio Astronomico di Capodimonte, Via Moiariello 16, I-80131 Napoli, Italy
Received 2017 February 16; revised 2017 March 21; accepted 2017 March 28; published 2017 April 10

Abstract

Since galaxy clusters sit at the high end of the mass function, the number of galaxy clusters both massive and concentrated enough to yield particularly large Einstein radii poses useful constraints on cosmological and structure formation models. To date, less than a handful of clusters are known to have Einstein radii exceeding $\sim 40''$ (for a source at $z_s \simeq 2$, nominally). Here, we report an addition to that list of the Sunyaev–Zel'dovich (SZ) selected cluster, PLCK G287.0+32.9 ($z = 0.38$), the second-highest SZ-mass (M_{500}) cluster from the Planck catalog. We present the first strong-lensing analysis of the cluster, identifying 20 sets of multiply imaged galaxies and candidates in new *Hubble Space Telescope* (*HST*) data, including a long, $l \sim 22''$ giant arc, as well as a quadruply imaged, apparently bright (magnified to $J_{\rm F110W} = 25.3$ AB), likely high-redshift dropout galaxy at $z_{\rm phot} = 6.90$ [6.13–8.43] (95% C.I.). Our analysis reveals a very large critical area (1.55 arcmin^2, $z_s \simeq 2$), corresponding to an effective Einstein radius of $\theta_E \sim 42''$. The model suggests the critical area will expand to 2.58 arcmin^2 ($\theta_E \sim 54''$) for sources at $z_s \sim 10$. Our work adds to recent efforts to model very massive clusters toward the launch of the *James Webb Space Telescope*, in order to identify the most useful cosmic lenses for studying the early universe. Spectroscopic redshifts for the multiply imaged galaxies and additional *HST* data will be necessary for refining the lens model and verifying the nature of the $z \sim 7$ dropout.

Key words: galaxies: clusters: general – galaxies: clusters: individual (PLCK G287.0+32.9) – gravitational lensing: strong

1. Introduction

Galaxy clusters are the most massive gravitationally bound objects in the universe, sitting at the high end of the mass function. Their total masses and mass profiles can be inferred in various complementary ways, including from cluster galaxy kinematics (Diaferio & Geller 1997), weak lensing (WL; Bartelmann & Schneider 2001), X-ray measurements (Sarazin 1986), or the Sunyaev–Zel'dovich effect (Sunyaev & Zeldovich 1972).

The abundance of the most massive clusters is important for scaling the mass function and probing cosmological models. *N*-body numerical simulations predict a universal mass profile form for virialized dark matter (DM) halos (e.g., Navarro et al. 1996), with increasing concentrations toward lower redshifts (as structure evolves) and for smaller masses (Duffy et al. 2008). Generally, the Einstein radius of a lens increases with its overall mass (explicitly, with the inner projected mass density) and with concentration (Sadeh & Rephaeli 2008). Given the shape of the concentration–mass relation, more massive, highly concentrated clusters become rarer. Assuming a mass function and a cosmological model, predictions for the distribution of Einstein radii in the universe can be made (Oguri & Blandford 2009; Waizmann et al. 2012; Redlich et al. 2014). Indeed, more factors can play an important role in determining the actual critical area size, such as the effective ellipticity and distribution of projected substructure (Redlich et al. 2012), or the halo's triaxiality. These factors can be accounted for statistically so that the comparison of the abundance of large lenses to ΛCDM predictions remains interesting.

To date, less than a handful of clusters are known to have critical areas exceeding 1.4 arcmin^2 for $z_s = 2$, i.e., an effective Einstein radius (defined as $\sqrt{A/\pi}$, with A being the critical area) exceeding $40''$ (and only few others are known with such a large critical area even for high-redshift sources). The largest strong lens currently known, with $\theta_E \sim 55''$ (Zitrin et al. 2009a), is MACS J0717.5+3745, a merging, massive (Medezinski et al. 2013), X-ray selected (Ebeling et al. 2010) galaxy cluster at $z = 0.55$. In fact, most massive clusters with known large Einstein radii have been chosen for follow-up based on optical classification (e.g., richness and luminosity), or X-ray measurements (Ebeling et al. 2010). However, with the recent abundance of SZ data and related cluster catalogs, such as those from Planck (Planck Collaboration et al. 2011a), the South Pole Telescope (SPT; Vanderlinde et al. 2010), and the Atacama Cosmology Telescope (ACT; Hasselfield et al. 2013), more potentially massive galaxy clusters have been detected.

Here, we present the first strong-lensing (SL) analysis of the Planck galaxy cluster PLCK G287.0+32.9 (PLCKG287

[10] Einstein Fellow.

hereafter), which has the second-highest SZ-inferred mass in the Planck catalog[11] ($M_{\rm SZ,500} = 13.89^{+0.53}_{-0.54} \times 10^{14}\,M_{\odot}$; Planck Collaboration et al. 2015).

This Letter is organized as follows: in Section 2, we summarize the observations and data reduction. In Section 3, we review the SL modeling of the cluster. In Section 4, we discuss the analysis results and their potential implications, and in Section 5, we conclude the work. Throughout, we use a standard ΛCDM cosmology with $\Omega_{\rm m0} = 0.3$, $\Omega_{\Lambda 0} = 0.7$, $H_0 = 100\,h$ km s^{-1}Mpc^{-1}, and $h = 0.7$. Magnitudes are given using the AB convention. $1''$ equals 5.21 kpc at the redshift of the cluster. Unless noted otherwise, errors are 1σ.

2. Target, Data, and Observations

PLCGK287 was discovered in early SZ observations by the Planck telescope (Planck Collaboration et al. 2011a). Follow-up X-ray observations with *XMM-Newton* yield a temperature of $T_{\rm X} = 12.86 \pm 0.42$ keV and mass of $M_{500} = 15.72 \pm 0.27 \times 10^{14}\,h_{70}^{-1}\,M_{\odot}$ (Planck Collaboration et al. 2011b).

The cluster was found to show also a non-thermal radio emission characterized by a double relic, indicating the system has undergone a recent major merger (Bagchi et al. 2011; Bonafede et al. 2014). The projected separation of the double radio relic is ∼4 Mpc, the largest known at comparable redshifts. From the *XMM-Newton* data a separation of ∼400 kpc is measured between the cluster BCG and the X-ray emission peak, providing additional evidence for merger activity.

PLCKG287 was previously imaged with the WFI on the 2.2 m MPG/ESO telescope in VRI filters. In a systematic WL study of SZ-selected clusters, Gruen et al. (2014; see also K. Finner et al. 2017, in preparation) confirmed the large mass estimates from SZ and X-ray and found the system to be the most massive among their sample, with $M_{\rm WL,500} = 19.5^{+3.3}_{-3.2} \times 10^{14}\,h_{70}^{-1} M_{\odot}$. In these optical data, several arc-like features were identified, spread out over a large field around the cluster core, with a radius exceeding an arcminute.

Following these findings, we obtained *Hubble Space Telescope* (*HST*) data in Cycle 23 to perform a dedicated SL analysis of this cluster (PI: Seitz, program ID 14165). PLCKG287 was observed on 2016 August 3 in the optical, ACS bands F475W, F606W, and F814W, with total exposure times of 1, 1, and 2 orbits, respectively. The cluster was also observed on 2016 May 18 with the WFC3/IR F110W filter, with four exposures per orbit over four orbits, centered on two locations, and adopting a half-pixel dither pattern. Data reduction was performed using advanced drizzle techniques (Koekemoer et al. 2011), including CR rejection, full astrometric alignment, weighting by the inverse variance, and drizzling, to produce the final set of mosaics.

We ran SExtractor (Bertin & Arnouts 1996) in dual-image mode to obtain the photometry of objects in the cluster field, using the F814W image as reference. Red-sequence cluster members, needed for our modeling, were chosen by a color–magnitude diagram, using the F814W and F606W filters, down to 23 AB. We then ran the Bayesian Photometric Redshift program (BPZ; Benítez 2000) with the photometric catalogs as input, to derive redshift estimates and help in the identification of multiple images.[12]

We had also observed PLCKG287 with VIMOS[13] on the VLT/UT3 (Le Fèvre et al. 2003) in service mode on four nights in 2015 February–March. We used the medium-resolution red grism and the GG475 filter, covering the ≈5000–10000 Å spectral range, with a resolution of ≈600. A total of twenty 1135 s exposures were obtained. These data have been reduced with a mix of custom pipeline and IRAF tasks (*apall, onedspec*). IRAF *rvsao* (Kurtz & Mink 1998) was used to estimate the redshifts. From ⩾220 member galaxies we estimate $z = 0.380$ for the cluster redshift (updating the $z = 0.39$ Planck estimate).

We cross-check our red-sequence selection with the VIMOS data to maximize the number of verified members included and remove red non-members. Out of the 248 red-sequence galaxies we consider members for the modeling, 35 within the *HST* FOV are spectroscopically confirmed. Additional objects suspected as interlopers in a visual inspection were removed.

3. Lens Model

We use the light-traces-mass (LTM) method by Zitrin et al. (2009b; see also Broadhurst et al. 2005; Zitrin et al. 2015) for the SL analysis of PLCKG287.

The photometry of red-sequence cluster galaxies (Section 2) is the starting point for the model. A power-law surface mass–density distribution is assigned to each galaxy, scaled in proportion to its luminosity (we use here the F606W magnitudes for reference). For the BCGs we typically assign *elliptical* power-law surface mass–density distributions with a core. The power-law exponent is the same for all galaxies and is the first free parameter of the model. The resulting map from the superposition of these galaxies is then smoothed with a Gaussian kernel, whose size is the second free parameter. The smoothed map constitutes the DM component of our model. The two components are then added with a relative weight, which is also iterated for, and scaled with an overall normalization that is the fourth free parameter. To allow for further flexibility, we also add a two-parameter external shear. The total number of free parameters principally is thus six. In addition, we typically also allow for the weight (and possibly core radius and ellipticity) of the brightest galaxies to be freely optimized in the minimization procedure.

Using preliminary LTM models, a method that has been shown to excel in predicting the appearance of multiply imaged galaxies (e.g., Broadhurst et al. 2005; Zitrin et al. 2009a, 2009b), we iteratively identify 20 sets of multiple images and candidates in the *HST* data (Section 2; see Figure 3). We set their redshift to the corresponding, best-value photometric redshifts, and use them as constraints for constructing the final model presented here. We only fix the redshifts for systems with relatively secure estimates (dropouts, or those where the photo-z agrees well among the different multiple images). The redshifts of the other systems were left free to be optimized in the minimization, as indicated in Table 1 listing the multiple images.

For the two central BCGs, we assign ellipticity values measured by SExtractor. We leave the weight of the two central BCGs, and two other bright galaxies, to be optimized in the minimization procedure.

[11] PSZ1; this is Mass_YZ_500, an SZ-mass proxy based on X-ray calibration of scaling relations.

[12] We also generated a version with the F110W image as reference.

[13] Programme 094.A-0529.

Table 1
Multiple Images and Candidates

Arc ID	R.A.	Decl.	$z_{\rm phot}$ [95% C.I.]	$z_{\rm model}$ [95% C.I.]	Comments
1.1	11:50:49.448	−28:05:02.060	3.76 [3.29–4.23]	=3.75	Radial image
1.2	11:50:49.054	−28:05:04.792	3.72 [3.26–4.18]	″	″
2.1	11:5054.201	−28:05:52.064	1.67 [1.41–1.93]	1.38 [1.30–1.60]	Other iterations yield $z_{\rm phot}\sim 2.3$
2.2	11:50:54.060	−28:05:54.105	1.82 [1.54–2.10]	″	″
2.3	11:50:52.844	−28:06:03.226	1.67 [1.41–1.93]	″	″
3.1	11:50:51.549	−28:05:39.538	2.81 [0.04–3.18]	1.34 [1.21–1.46]	…
3.2	11:50:51.197	−28:05:42.271	0.35 [0.09–3.12]	″	…
3.3	11:50:53.830	−28:05:10.648	0.93 [0.13–2.56]	″	…
4.1	11:50:50.800	−28:05:43.124	1.04 [0.84–1.24]	2.55 [2.14–2.92]	…
4.2	11:50:50.667	−28:05:44.562	1.17 [0.96–1.41]	″	…
c4.3	11:50:54.469	−28:05:04.469	0.97 [0.13–1.25]	″	…
5.1	11:50:50.890	−28:04:31.287	2.55 [0.07–2.93]	1.53 [1.31–1.89]	…
5.2	11:50:51.303	−28:04:31.069	2.23 [0.18–2.81]	″	…
c5.3	11:50:47.248	−28:05:16.134	1.86 [1.58–2.41]	″	…
c5.3	11:50:46.243	−28:05:30.772	3.14 [1.14–3.57]	″	Most likely according to the model
c5.3	11:50:45.865	−28:05:39.327	0.46 [0.13–3.31]	″	…
c6.1	11:50:47.021	−28:04:51.560	4.43 [3.90–4.96]	…	…
c6.2	11:50:47.232	−28:04:42.851	4.51 [0.68–5.05]	…	…
7.1	11:50:49.252	−28:04:23.606	3.32 [2.90–3.74]	=3.4	…
7.2	11:50:52.875	−28:04:23.606	3.47 [3.03–3.91]	″	…
7.3	11:50:51.702	−28:05:17.047	3.33 [2.91–3.79]	″	…
7.4	11:50:46.982	−28:05:41.706	3.52 [3.08–3.96]	″	…
8.1	11:50:52.743	−28:04:48.339	2.44 [1.88 2.78]	0.99 [0.92–1.06]	…
8.2	11:50:51.290	−28:05:12.952	3.04 [3.59–3.44]	″	Other iterations yield $z_{\rm phot}\sim 2.4$
8.3	11:50:49.593	−28:05:22.032	1.06 [0.45–1.66]	″	″
c9.1	11:50:50.430	−28:05:26.016	0.87 [0.59–2.78]	…	…
c9.2	11:50:50.200	−28:05:27.985	0.85 [0.22–4.06]	…	Nearby parts yield $z_{\rm phot}\sim 2.5$
10.1	11:50:44.942	−28:05:02.578	0.98 [0.79–1.17]	0.89 [0.71–0.91]	…
10.2	11:50:44.929	−28:05:04.072	0.97 [0.78–1.16]	″	…
10.3	11:50:44.993	−28:05:06.556	1.02 [0.82–1.22]	″	…
c11.1	11:50:44.089	−28:05:09.461	0.10 [0.00–2.54]	…	…
c11.2	11:50:44.063	−28:05:10.642	0.09 [0.00–3.09]	…	…
c11.3	11:50:44.202	−28:05:17.428	0.09 [0.00–2.86]	…	…
12.1	11:50:43.705	−28:05:18.794	3.43 [3.00–3.86]	=3.4	…
12.2	11:50:43.598	−28:05:13.836	3.47 [3.03–3.91]	″	…
c12.3	11:50:43.603	−28:05:13.483	3.36 [2.93–3.79]	″	…
c12.4	11:50:43.821	−28:05:00.398	…	″	Blended with another object
c13.1	11:50:55.879	−28:04:25.578	0.81 [0.20–4.98]	…	…
c13.2	11:50:55.428	−28:04:19.980	4.16 [3.65–4.67]	…	…
c13.3	11:50:54.995	−28:04:14.134	4.77 [4.21–5.33]	…	…
14.1	11:50:55.751	−28:04:04.016	0.77 [0.60–1.05]	…	Not used as constraint
14.2	11:50:55.855	−28:04:05.816	0.92 [0.60–1.11]	…	″
14.3	11:50:56.109	−28:04:07.315	0.75 [0.50–0.92]	…	″
c15.1	11:50:50.470	−28:03:54.703	0.54 [0.39–0.69]	…	Other iterations yield $z_{\rm phot}\sim 3$
c15.2	11:50:50.239	−28:03:54.937	0.47 [0.33–0.61]	…	″
16.1	11:50:53.949	−28:06:17.632	2.97 [0.19–3.36]	…	Not used as constraint
16.2	11:50:53.919	−28:06:17.939	…	…	″
16.3	11:50:53.588	−28:06:19.559	3.37 [2.74–3.80]	…	″
c17.1	11:50:45.396	−28:05:00.931	0.83 [0.12–3.87]	…	…
c17.2	11:50:45.377	−28:05:08.390	3.19 [0.41–3.72]	…	Nearby parts yield $z_{\rm phot}\sim 3.7$–4
c18.1	11:50:45.271	−28:05:15.966	0.59 [0.12–3.46]	…	…
c18.2	11:50:45.255	−28:05:21.258	3.40 [0.69–3.83]	…	…
c17/18	11:50:46.578	−28:04:23.945	0.71 [0.47–0.97]	…	…

Table 1
(Continued)

Arc ID	R.A.	Decl.	$z_{\rm phot}$ [95% C.I.]	$z_{\rm model}$ [95% C.I.]	Comments
19.1	11:50:49.203	−28:04:14.689	6.90 [6.13–8.43]	=6.9	Dropout, not detected in ACS bands
19.2	11:50:52.784	−28:04:17.603	6.90 [6.13–8.43]	″	″
19.3	11:50:51.936	−28:05:16.296	6.90 [6.13–8.54]	″	″
19.4	11:50:46.185	−28:05:44.875	6.94 [6.16–8.32]	″	″
c19.5	11:50:50.443	−28:04:53.959	1.35 [0.95–8.83]	″	″, in BCG's light
c20.1	11:50:50.632	−28:05:03.137	0.98 [0.07–1.71]	…	In BCG light, radial image
c20.2	11:50:50.521	−28:05:00.919	5.88 [1.60–6.55]	…	″

Note. Column 1: ID . "c" stands for candidate where identification was more ambiguous, and image was not used as a constraint. Columns 2 and 3: R.A. and decl. in J2000.0. Column 4: photometric redshift and 95% C.L. from BPZ. Column 5: predicted and 95% C.L. redshift by our lens model, for systems whose redshift was left to be optimized in the minimization (otherwise, a fixed value is listed). Column 6: comments.

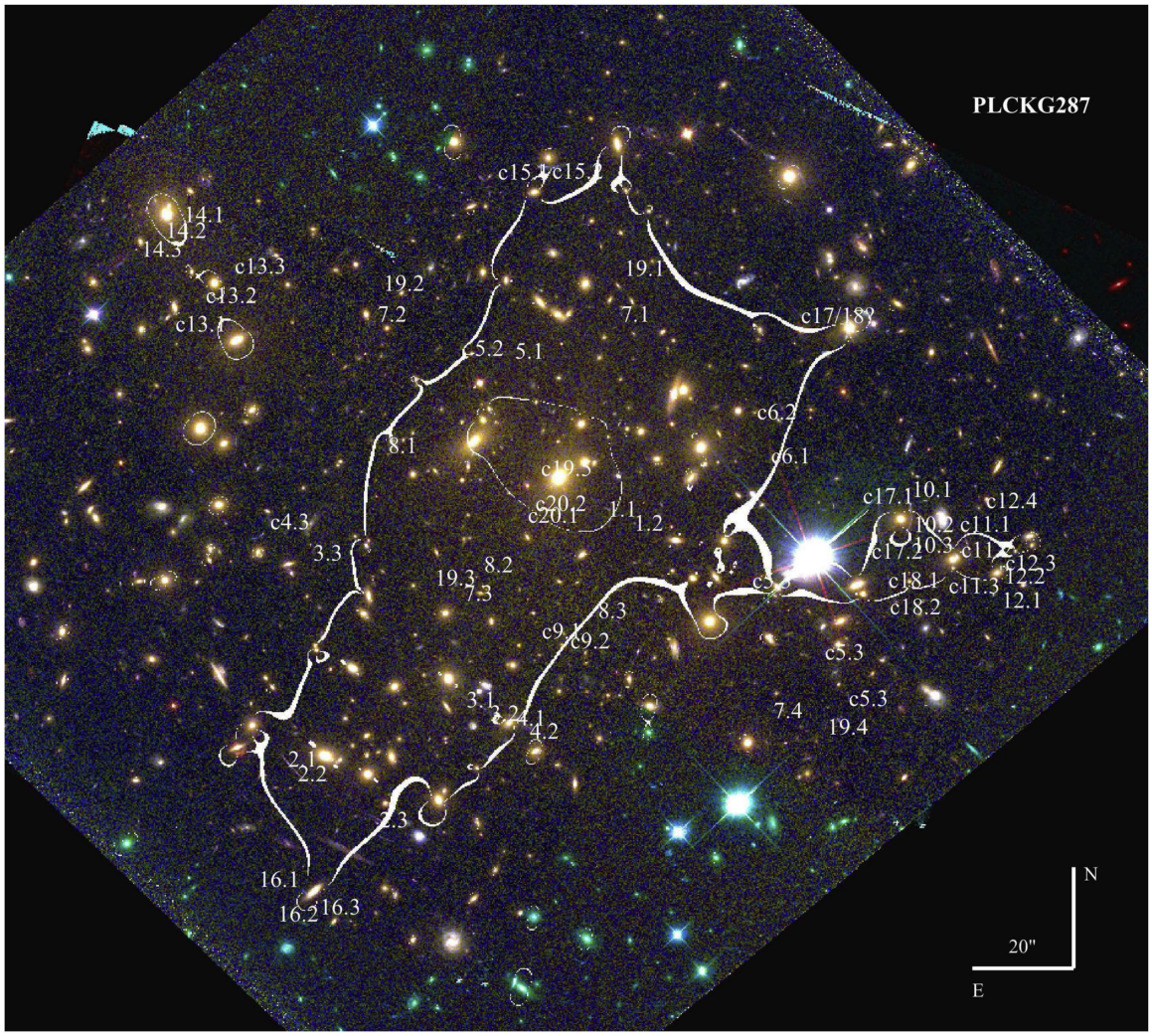

Figure 1. Galaxy cluster PLCKG287. The critical curves from our model are marked in white for a source at $z_{\rm phot} \simeq 3.4$, enclosing an area with an effective Einstein radius of $\theta_{\rm E} = 49 \pm 5''$. The multiple images we identify are numbered and marked on the image ("c" stands for "candidate"). Image is constructed using R = F110W, G = F814W+F606W, and B = F475W.

The minimization of the model is performed with several thousand Monte Carlo Markov Chain steps, through a χ^2 criterion quantifying the reproduction of the multiple image positions (adopting a positional uncertainty of $0\farcs5$, or $1\farcs4$ when calculating the errors). The final model has an image reproduction rms of $1\farcs9$. The resulting critical curves ($z_s = 3.4$) are seen in Figure 1 along with the multiply imaged galaxies. The best-model mass map and profile are seen in Figure 2.

It should be noted that our results are based only on four-band photometric redshifts for the multiple images, and thus may vary strongly depending on the true redshift of the sources. In addition, there is some ambiguity with respect to few potential multiple images (Figure 1, Table 1; for example,

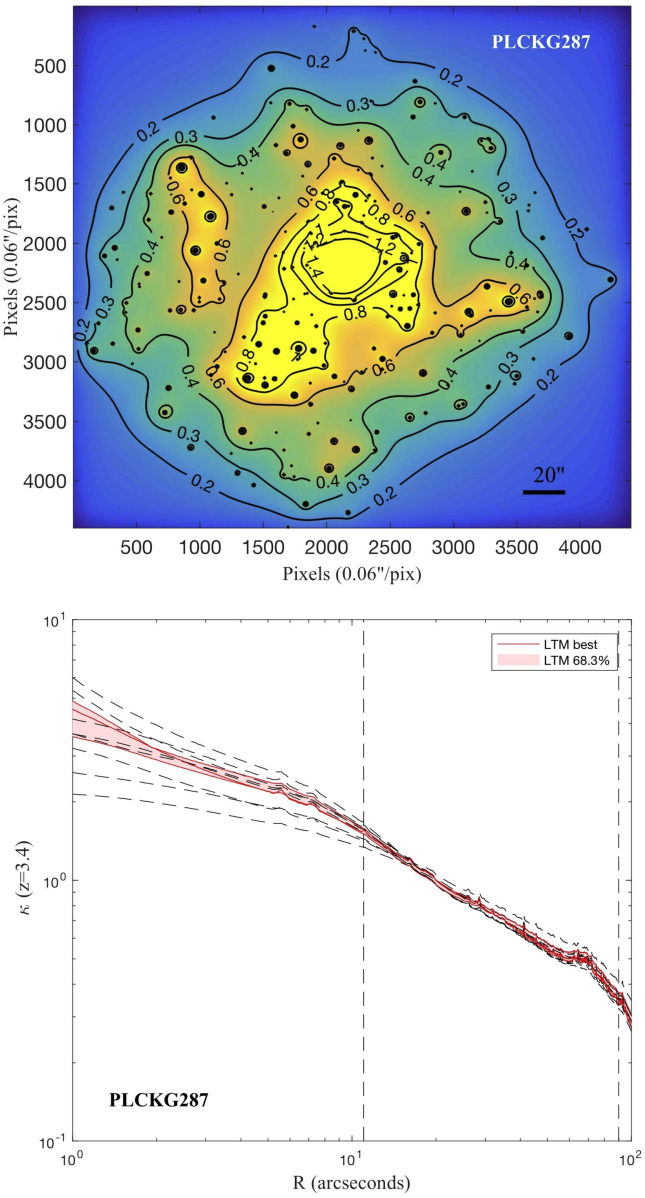

Figure 2. Top: map of κ, the projected surface mass density in units of the critical density for lensing, scaled to the redshift of system 7, $z_s \simeq 3.4$. Bottom: the corresponding radially averaged mass density profile. The profile slope in the range [1, 84] arcseconds (∼440 kpc, about twice the Einstein radius) is $d \log \kappa / d \log \theta \simeq -0.55$, similar to other well-known lensing clusters (Figure 7 in Zitrin et al. 2015). Vertical dashed lines mark the area in which there are multiple-image constraints. The black, dashed profile lines demonstrate the range spanned by models run with different choices of fixed source redshifts.

which candidates are the true, third counter images of systems 5, 12, or 15). It is also at present unclear what the nature of the 22″ long giant arc is (systems c17 and c18), whether or not it is multiply imaged, and whether or not there is an additional counter image north of the arc. Similarly, if candidate system 13 is a multiply imaged galaxy, this means that the eastern "arm" seen in the surface density map in Figure 2 creates a local critical curve larger that the simple LTM assumption yields. On the other hand, if systems 10 and 11 have a notably higher redshift than our current estimates imply, it might mean the western arm is in fact smaller and consists only of local critical curves around the respective galaxies. Additional uncertainty arises from the bright galaxy at [R.A., decl.] = [11:50:46.747, −28:03:56.560] that was chosen by our red-sequence criteria, but the VIMOS data suggest it is not officially a cluster member (it has a >10,000 km s^{-1} lower velocity than the cluster average). The galaxy seems to contribute to some extent to the lensing signal, though, and so we leave it in the modeling but with a reduced weight. The lack of obvious multiple-image systems around that northern tip suggests this choice is reasonable.

We did not use candidate images as constraints, and, in most ambiguities listed above, we generally favored the conservative choice, so that the actual critical area may, if anything, be larger than our estimate in Section 4.

4. Results and Discussion

Our SL analysis reveals a very big lens, with a critical area of 1.55 arcmin^2, for $z_s \simeq 2$, corresponding to an effective Einstein radius of $\theta_{\rm E} \simeq 42 \pm 4''$. The mass enclosed within these curves is $3.1 \pm 0.5 \times 10^{14}\, M_\odot$. For $z_s \simeq 3.4$, for example, the critical curves expand further as expected, reaching an effective Einstein radius of $\theta_{\rm E} \sim 49''$, and for $z_s \sim 10$, our model suggests they would reach $\theta_{\rm E} \sim 54''$.

To examine the effect of lack of accurate redshifts we ran four other models with significantly different combinations of fixed redshifts. The Einstein radii estimates between the different models is within 10% of each other, and the enclosed masses agree to 15%. The mass profile and correspondingly, predicted redshifts, are more sensitive to the exact redshifts initially adopted, and typically agree to 2σ–3σ.

Few clusters are known to have Einstein radii above 40″ (for typical source redshifts of $z_s \sim 2$). These include the largest known gravitational lens, MACS J0717.5+3745, included also in the Cluster Lensing And Supernova with Hubble (CLASH; Postman et al. 2012) and Hubble Frontier Fields (HFF; Lotz et al. 2016) programs, with $\theta_{\rm E} \sim 55''$ (Zitrin et al. 2009a); Abell 1689 ($\theta_{\rm E} \sim 45''$; Broadhurst et al. 2005); and the HFF cluster Abell 370 (∼40″; Richard et al. 2010). Also worth mentioning is RCS2 J232727.6−020437, for which Sharon et al. (2015) find $\theta_{\rm E} \simeq 40''$ for $z_s \simeq 3$ (but smaller—i.e., 26″—as expected, for another source at $z \simeq 1.4$).

The distribution of Einstein radii, and in particular the high end of this distribution, is important to characterize, as the largest and most massive lenses help to probe cosmological models and structure formation scenarios (Oguri & Blandford 2009; Waizmann et al. 2012; Redlich et al. 2014). The high concentrations and large Einstein radii found for several massive clusters have been previously claimed to challenge ΛCDM (Broadhurst & Barkana 2008; Broadhurst et al. 2008), although updated analyses (and accounts of projection biases) have alleviated this tension (Merten et al. 2015; Umetsu et al. 2016). In a similar fashion, the amount of substructure within massive clusters can also be compared to numerical simulations and expectations from ΛCDM (Jauzac et al. 2016; Schwinn et al. 2017). Given its extreme properties, PLCKG287 is another useful laboratory for similar studies.

Most of the impressive lenses known to date, including the $\theta_{\rm E} > 40''$ lenses mentioned above as well as those observed by the CLASH and HFF programs, and that were found to be magnifying many high-redshift lensed galaxies (e.g., Bradley et al. 2014; Kawamata et al. 2016 and references therein), were selected for *HST* follow-up mostly due to their optical (e.g., richness) or X-ray signals. X-ray selection in particular has proved to be an excellent probe for locating merging clusters

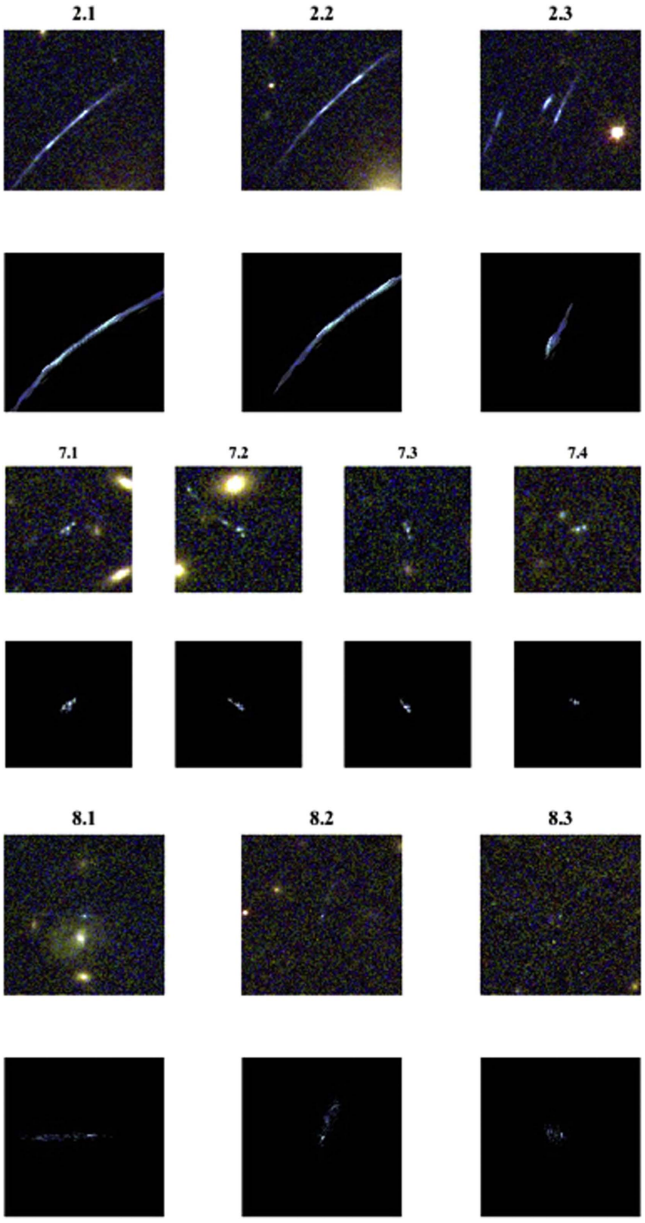

Figure 3. Reproduction of multiple images by our model. In each case, we delens one of the images (2.2, 7.1, and 8.2, explicitly) to the source plane and back to the image plane to compare to the other images of that system. As can be seen, the orientation and internal details of the predicted images (bottom rows) resemble those of the real images identified in the predicted location in the data (upper rows), supporting the identification.

with large critical curves (Ebeling et al. 2010; Zitrin et al. 2015), as mergers tend to boost the critical area. Here, we concentrate on an SZ-selected cluster, which has the second-highest $M_{\rm SZ}$ estimate in the Planck cluster catalog. In addition to our observations, PLCKG287 will be observed in the ongoing Reionization Lensing Cluster Survey (RELICS; PI: Coe), an *HST* program to observe a large set of mainly SZ-mass selected clusters, designed to find high-redshift, bright dropout galaxies in the reionization epoch.

Indeed, recent SZ surveys have expanded our massive-cluster sample. One such notable example is ACT-CL J0102-4915, the "El Gordo" cluster, a high-redshift ($z = 0.87$) and likely the most massive, hottest, most X-ray luminous and brightest SZ effect cluster known at $z > 0.6$ (Menanteau et al. 2012; Jee et al. 2014). Zitrin et al. (2013) performed the first SL analysis of this cluster, revealing a large lens with a critical area exceeding $\simeq$1.4 arcmin^2 for high-redshift sources ($z_s \gtrsim 4$). This shows the power of SZ massive-cluster selection, especially at higher redshifts, much due to the fact that the SZ signal is not redshift dependent (nonetheless, X-ray and optical/near-infrared observations have also revealed high-redshift clusters, including out to $z > 1$ and $z > 2$, respectively; Rosati et al. 2009; Strazzullo et al. 2016).

One interesting question is whether there is a preferred selection that leads to larger or "better" strong lenses, particularly for high-z applications. Scaling relations between X-ray, SZ, luminosity, richness, and lensing masses are well established, and characterized with increasing precision (e.g., Rozo et al. 2014). However, high total mass is not sufficient to guarantee a large critical area, which is dependent on the exact central projected mass density distribution (Redlich et al. 2012). In this relation, efforts have been made in recent years to detect clusters with large critical areas more directly, based on the luminosity distribution of red cluster member galaxies, and calibrated with well-studies lensing clusters (Wong et al. 2012; Zitrin et al. 2012). It will be interesting to compare these selections to other probes (richness, SZ, X-ray) once relevant *HST* data become available.

Among the multiply imaged galaxies we detect in PLCKG287, noteworthy is a likely high-redshift dropout, detected only in F110W. We identify four multiple images of this galaxy (Figure 4). An additional, demagnified fifth one is predicted next to the BCG core, and we list here one potential candidate (system 19; Table 1). The photometric redshifts for all four magnified images of the galaxy agree well, $z_{\rm phot} = 6.9$ [6.13–8.43] (95% C.I.) and are corroborated by our lens model: the system symmetry follows that of system 7 at $z \simeq 3.4$, but at a larger radius (and requires a higher lensing distance ratio) so that the higher-redshift nature of this object is also supported geometrically from lensing.

Due to its relative brightness (observed apparent magnitudes of $J_{\rm F110W} = 25.3$–25.5 AB for the four images), this galaxy presents a promising case for the challenging spectroscopic follow-up of high-redshift sources. In addition to its brightness, the SNR of such observations can be significantly increased by observing the four magnified images simultaneously. Using the magnification factors implied by our model (μ between 2.4 and 4.8), the source intrinsic (i.e., demagnified) apparent magnitude is $J_{\rm F110W} \sim 26.7 \pm 0.4$ AB, and the intrinsic half-light radius is 0.4 ± 0.14 kpc, where the errors represent the range from the four images and their magnification values. In future iterations, the source's relative magnifications can also be used as additional constraints for the model.

5. Summary

Galaxy clusters constitute great cosmic telescopes. Extensive lensing surveys have taught us that essentially all massive clusters act as useful gravitational lenses, distorting, magnifying, and multiply imaging objects behind them. This has allowed us to construct dozens of mass maps and enabled the continuous discovery of hundreds of magnified, high-redshift galaxies. However, even with significant *HST* time devoted to recent lensing surveys, the data (and corresponding lensing models) currently available sample only a relatively small part of all massive clusters. There are expected to be a dozen to several dozen massive clusters in the sky with $\theta_{\rm E} > 40''$

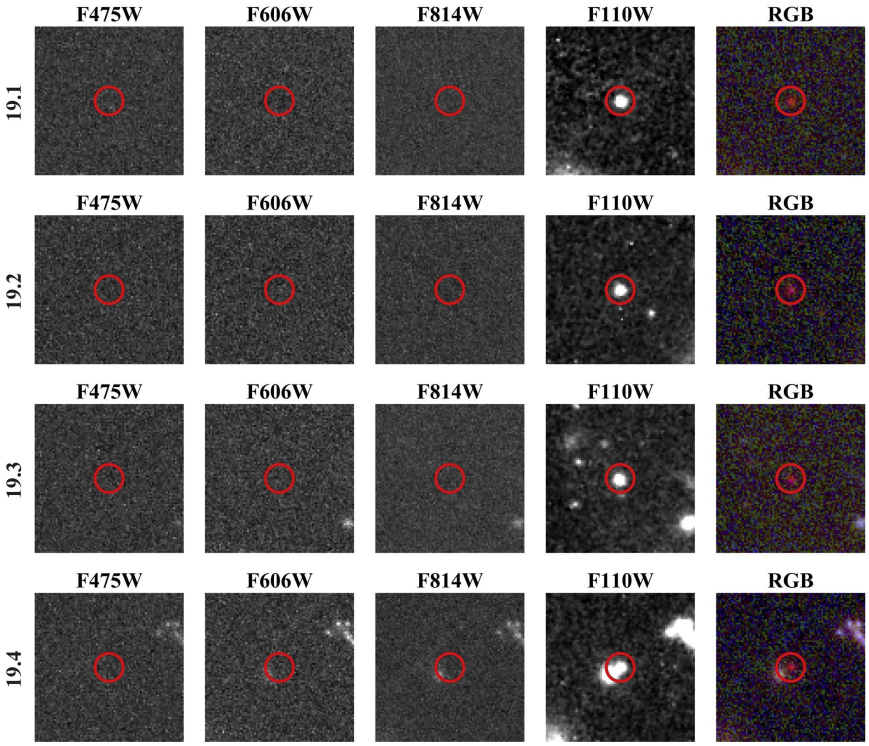

Figure 4. Quadruply lensed, dropout high-redshift candidate (system 19). All four images of the dropout galaxy are detected only in the F110W band. Squares are 5″ on a side. Red circle radius is ≃0.″5.

(Oguri & Blandford 2009; Zitrin et al. 2012), and finding the most massive lenses and the best cosmic telescopes among these is important for studying the cosmological model and structure formation and evolution, and for maximizing the chances to detect increasingly fainter objects at higher redshifts.

Here, we modeled the massive cluster PLCKG287 and identified 20 multiple-image families and candidates, including an apparently bright ($J_{\rm F110W} = 25.3$AB), quadruply imaged $z_{\rm phot} \sim 7$ galaxy. Our analysis reveals a large Einstein radius of $42 \pm 4''$ for $z_s \simeq 2$, and $54 \pm 5''$ for $z_s \sim 10$, adding to the short list of only a few similarly large lenses. Our results are based solely on photometric redshifts, and so a refinement of the model is warranted when more data—in particular, spectroscopic redshifts—become available (however, given the redshift range already spanned by the multiply imaged galaxies, we consider the Einstein radius robust). Interestingly, in contrast to most impressive lenses we are familiar with to date, that are X-ray or optically selected, and similar to the notable example of *El Gordo*, this cluster is SZ-selected. It will be intriguing to see in the near future if a certain selection (such as SZ, X-ray, luminosity, richness, or other, more direct lensing-based optical methods) is most efficient in locating the largest strong lenses and those best suited for studying the early universe.

We thank the anonymous reviewer of this work for very useful comments. This work is based on observations made with the NASA/ESA Hubble Space Telescope. Support for program ID 14165 (PI: Seitz) was provided by NASA from the Space Telescope Science Institute (STScI), which is operated by the Association of Universities for Research in Astronomy, Inc. under NASA contract NAS 5-26555. S.S. thanks the DFG Transregio 33 "The Dark Universe" and the DFG cluster of excellence "Origin and Structure of the Universe" for support. Support for D.G. was provided by NASA through the Einstein Fellowship Program, grant PF5-160138. A.M. and M.N. acknowledge support by PRIN-INAF 2014 1.05.01.94.02. IRAF is distributed by the National Optical Astronomy Observatories, which are operated by the Association of Universities for Research in Astronomy, Inc., under cooperative agreement with the National Science Foundation. IRAF rvsao was developed at the Smithsonian Astrophysical Observatory Telescope Data Center.

References

Bagchi, J., Sirothia, S. K., Werner, N., et al. 2011, ApJL, 736, L8
Bartelmann, M., & Schneider, P. 2001, PhR, 340, 291
Benítez, N. 2000, ApJ, 536, 571
Bertin, E., & Arnouts, S. 1996, A&AS, 117, 393
Bonafede, A., Intema, H. T., Brüggen, M., et al. 2014, ApJ, 785, 1
Bradley, L. D., Zitrin, A., Coe, D., et al. 2014, ApJ, 792, 76
Broadhurst, T., Benítez, N., Coe, D., et al. 2005, ApJ, 621, 53
Broadhurst, T., Umetsu, K., Medezinski, E., Oguri, M., & Rephaeli, Y. 2008, ApJL, 685, L9
Broadhurst, T. J., & Barkana, R. 2008, MNRAS, 390, 1647
Diaferio, A., & Geller, M. J. 1997, ApJ, 481, 633
Duffy, A. R., Schaye, J., Kay, S. T., & Dalla Vecchia, C. 2008, MNRAS, 390, L64
Ebeling, H., Edge, A. C., Mantz, A., et al. 2010, MNRAS, 407, 83
Gruen, D., Seitz, S., Brimioulle, F., et al. 2014, MNRAS, 442, 1507
Hasselfield, M., Hilton, M., Marriage, T. A., et al. 2013, JCAP, 7, 008
Jauzac, M., Eckert, D., Schwinn, J., et al. 2016, MNRAS, 463, 3876
Jee, M. J., Hughes, J. P., Menanteau, F., et al. 2014, ApJ, 785, 20
Kawamata, R., Oguri, M., Ishigaki, M., Shimasaku, K., & Ouchi, M. 2016, ApJ, 819, 114
Koekemoer, A. M., Faber, S. M., Ferguson, H. C., et al. 2011, ApJS, 197, 36
Kurtz, M. J., & Mink, D. J. 1998, PASP, 110, 934
Le Fèvre, O., Saisse, M., Mancini, D., et al. 2003, Proc. SPIE, 4841, 1670
Lotz, J. M., Koekemoer, A., Coe, D., et al. 2016, ApJ, submitted (arXiv:1605.06567)
Medezinski, E., Umetsu, K., Nonino, M., et al. 2013, ApJ, 777, 43
Menanteau, F., Hughes, J. P., Sifón, C., et al. 2012, ApJ, 748, 7

Merten, J., Meneghetti, M., Postman, M., et al. 2015, ApJ, 806, 4
Navarro, J. F., Frenk, C. S., & White, S. D. M. 1996, ApJ, 462, 563
Oguri, M., & Blandford, R. D. 2009, MNRAS, 392, 930
Planck Collaboration, Ade, P. A. R., Aghanim, N., et al. 2011a, A&A, 536, A8
Planck Collaboration, Ade, P. A. R., Aghanim, N., et al. 2015, A&A, 581, A14
Planck Collaboration, Aghanim, N., Arnaud, M., et al. 2011b, A&A, 536, A9
Postman, M., Coe, D., Benítez, N., et al. 2012, ApJS, 199, 25
Redlich, M., Bartelmann, M., Waizmann, J.-C., & Fedeli, C. 2012, A&A, 574, A66
Redlich, M., Waizmann, J.-C., & Bartelmann, M. 2014, A&A, 569, A34
Richard, J., Kneib, J.-P., Limousin, M., Edge, A., & Jullo, E. 2010, MNRAS, 402, L44
Rosati, P., Tozzi, P., Gobat, R., et al. 2009, A&A, 508, 583
Rozo, E., Bartlett, J. G., Evrard, A. E., & Rykoff, E. S. 2014, MNRAS, 438, 78
Sadeh, S., & Rephaeli, Y. 2008, MNRAS, 388, 1759
Sarazin, C. L. 1986, RvMP, 58, 1
Schwinn, J., Jauzac, M., Baugh, C. M., et al. 2017, MNRAS, 467, 2913
Sharon, K., Gladders, M. D., Marrone, D. P., et al. 2015, ApJ, 814, 21
Strazzullo, V., Daddi, E., Gobat, R., et al. 2016, ApJL, 833, L20
Sunyaev, R. A., & Zeldovich, Y. B. 1972, CoASP, 4, 173
Umetsu, K., Zitrin, A., Gruen, D., et al. 2016, ApJ, 821, 116
Vanderlinde, K., Crawford, T. M., de Haan, T., et al. 2010, ApJ, 722, 1180
Waizmann, J.-C., Redlich, M., & Bartelmann, M. 2012, A&A, 547, A67
Wong, K. C., Ammons, S. M., Keeton, C. R., & Zabludoff, A. I. 2012, ApJ, 752, 104
Zitrin, A., Broadhurst, T., Bartelmann, M., et al. 2012, MNRAS, 423, 2308
Zitrin, A., Broadhurst, T., Rephaeli, Y., & Sadeh, S. 2009a, ApJL, 707, L102
Zitrin, A., Broadhurst, T., Umetsu, K., et al. 2009b, MNRAS, 396, 1985
Zitrin, A., Fabris, A., Merten, J., et al. 2015, ApJ, 801, 44
Zitrin, A., Menanteau, F., Hughes, J. P., et al. 2013, ApJL, 770, L15